Determining rotational temperatures from the OH(8-3) band, and a comparison with OH(6-2) rotational temperatures at Davis, Antarctica

F. Phillips[1], G. B. Burns[1], W. J. R. French[1], P. F. B. Williams[1], A. R. Klekociuk[1], and R. P. Lowe[2]

[1]Australian Antarctic Division, Kingston 7050, Tasmania, Australia
[2]Department of Physics and Astronomy, University of Western Ontario, London N6A3K7, Canada

Abstract. Rotational temperatures derived from the OH(8–3) band may vary by $\sim$18 K depending on the choice of transition probabilities. This is of concern when absolute temperatures or trends determined in combination with measurements of other hydroxyl bands are important. In this paper, measurements of the OH(8–3) temperature-insensitive Q/P and R/P line intensity ratios are used to select the most appropriate transition probabilities for use with this band. Aurora, airglow and solar and telluric absorption in the OH(8–3) band are also investigated. Water vapour absorption of $P_1(4)$, airglow or auroral contamination of $P_1(2)$ and solar absorption in the vicinity of $P_1(5)$ are concerns to be considered when deriving rotational temperatures from this band.

A comparison is made of temperatures derived from OH(6–2) and OH(8–3) spectra collected alternately at Davis (69° S, 78° E) in 1990. An average difference of $\sim$4 K is found, with OH(8–3) temperatures being warmer, but a difference of this magnitude is within the two sigma uncertainty limit of the measurements.

Key words. Atmospheric composition and structure (airglow and aurora; pressure, density, and temperature)

1 Introduction

Warming of the troposphere due to increases in greenhouse gas concentrations is associated with enhanced cooling in the stratosphere and mesosphere (Berger and Dameris, 1993; Portman et al., 1995; Akmaev and Fomichev, 1998, 2000). Several authors have used rotational temperatures derived from hydroxyl airglow emissions to investigate trends in the upper mesosphere (Golitsyn et al., 1996; Lysenko et al., 1999; Bittner et al., 2002; Burns et al., 2002; Espy and Stegman, 2002). Hydroxyl airglow emissions originate from a layer near 87 km with a mean thickness of 8 km (Baker and

Correspondence to: Gary Burns
(gary.burns@aad.gov.au)

Stair, 1988) and can be used as a proxy for kinetic temperature at $\sim$87 km (She and Lowe, 1998).

Hydroxyl airglow rotational temperatures are derived by comparing intensities of two or more lines from different upper rotational states, as per Eq. (1):

$$T = (hc/k)(F_b - F_a)/\ln[I_a A_b(2J_b' + 1)/I_b A_a(2J_a' + 1)] \qquad (1)$$

F_a, F_b are the energy levels of the initial rotational states (the energy level values as given by Coxon and Foster, 1982, are used); I_a, I_b are the emission intensities of the OH lines from different upper states; A_a, A_b are the transition probabilities; J_a', J_b' are the upper state, total angular momentum quantum numbers; and h, c and k are Planck's constant, the speed of light and Boltzmann's constant, respectively. Transition probabilities are used to apportion the percentage of the upper rotational states that decay via the transitions measured.

Hydroxyl bands are designated by transitions from an upper state, v' (=vibration quantum number), to a lower state, v'', as the OH(v'–v'') band. As Δv increases the bands become less intense and appear at lower wavelengths. The choice of band to monitor is thus generally selected based on the upper wavelength limit of the detector. The hydroxyl line nomenclature used in this paper is similar to that presented by Osterbrock and Martel (1992) and Osterbrock et al. (1996, 1997). A summary is presented in the Appendix.

Rotational temperatures have been derived from OH(6–2) spectra collected at Davis Station, Antarctica (69° S, 78° E) during 1990 and each winter since 1995 using a Czerny-Turner spectrometer (CTS, Burns et al., 2002). The OH(6–2) band near λ 840 nm is the brightest band that can be measured with GaAs photomultipliers. Greet et al. (1998) examined the minor spectral features, auroral and Fraunhofer contamination of the OH(6–2) P-branch to quantify uncertainties for climate studies.

Absolute values of derived hydroxyl rotational temperatures depend on the transition probabilities, A_a, A_b in Eq. (1). The discrepancy in published transition probabilities increases with higher Δv bands, resulting in increasing discrepancies in the determined temperatures (Turnbull

and Lowe, 1989; hereafter T&L). For example, Langhoff et al. (1986; hereafter LWR) OH(6–2) transition probabilities yield an average winter hydroxyl temperature at Davis of 206 K (Burns et al., 2002) compared with 211 K, if Mies (1974, hereafter Mies) transition probabilities are used and 218 K, if the T&L transition probabilities are used, giving differences of 5 K and 12 K, respectively. In comparison, for an analysis of the OH(8–3) band that returns a temperature of 206 K using the LWR probabilities, the corresponding temperature using the Mies OH(8–3) transition probabilities would be 213 K and 224 K for the T&L transition probabilities, giving differences of 7 K and 18 K, respectively. Intensity ratios of emissions from the same hydroxyl upper state are independent of the kinetic temperature. French et al. (2000) measured these temperature-independent ratios for the OH(6–2) band and compared them with ratios calculated using LWR, Mies and T&L transition probabilities. They found that LWR values were most compatible with the experimental measurements. Pendleton and Taylor (2002) provide a theoretical interpretation of the French et al. (2000) results. When comparing temperatures from different transitional bands or with temperatures derived by other methods, particularly bands with high Δv, care must be taken to ensure that the choice of transition probabilities does not introduce an offset in the hydroxyl temperatures.

Differences in hydroxyl rotational temperatures derived from different bands have been interpreted as providing evidence for a height variation of hydroxyl upper state vibrational levels. This is a possible source of hydroxyl temperature variability when different bands are measured. Theoretical considerations suggest the vertical distribution for $v'=1$ to $v'=9$ is 1 to 2 km (McDade, 1991). The average winter temperature gradient measured at Syowa (69° S, 39° E) using a sodium lidar is -1.7 K km^{-1}, at 87 km (Burns et al., 2003). The temperature difference due to variations in average altitudes is expected to be small for small $\Delta v'$.

The OH(8–3) band was commonly used for hydroxyl temperature measurements in past years (for example, Takahashi et al., 1974; Takahashi and Batista, 1981; Myrabo, 1984; Sivjee and Hamwey, 1987). In particular, hydroxyl airglow OH(8–3) band measurements have been made in Antarctica as early as 1979 (Stubbs et al., 1983; Williams, 1996). A desire to understand this spectral region, with the possibility of recovering more accurate rotational temperatures from early records, prompted this research.

In 1990 at Davis Station, Antarctica, spectra were collected alternately in the OH(8–3) and (6–2) region. In 1999, high-spectral-resolution, full-band OH(8–3) spectra were collected over a 5 week period. In this paper, these high-resolution spectra are used to identify possible auroral and Fraunhofer contamination, and the location of spectral features which may effect temperature determinations from the OH(8–3). Temperature-independent intensity ratios are determined from the high-resolution spectra and compared with the ratios predicted by published transition probabilities to determine which transition probabilities are most appropriate to use when determining rotational temperatures

in this band. Information gained from the high-resolution 1999 spectra is used to determine rotational temperatures from OH(8–3) spectra collected in 1990. These temperatures are compared with temperatures from alternately collected OH(6–2) spectra, derived using information on this band published by Greet et al. (1998) and French et al. (2000), to quantify differences which may influence temperature trends determined from combining measurements of these bands from different eras.

2 Instrumentation and data

Spectra were collected with a scanning Czerny-Turner spectrometer (CTS) at Davis during 1990 and 1999, using a cooled (-28°C) GaAs photomultiplier. The CTS has a 6° field-of-view (fov). An expanded description of the instrument is provided by Williams (1996).

Spectral response is determined by scanning a low brightness source (LBS) which uniformly illuminates the instrument's fov. The lamp is calibrated against a spectral standard at the Australian Measurement Laboratories. A total of 63 scans from four separate occasions were collected during 1999. The LBS intensities at $\lambda724$ nm and $\lambda740$ nm, the largest separation of lines compared, yielded a consistent calibration ratio to within 0.4%.

In April 1999, the CTS was aligned to the zenith and scanned OH(8–3) R-, Q-, and P-branches from $\lambda723.5$ to $\lambda740.5$ nm at intervals of 0.005 nm and an integration time of 0.5 s. Acquisition time for each spectrum was 32 min. An order-separating filter ($\lambda<475$ nm) limited observations to the first order. Rowland "ghosts" (Longhurst, 1957) of magnitudes 0.5% and 0.2%, displaced by 0.3 nm and 0.6 nm, respectively, were measured. An instrument profile of 0.086 nm full-width-at-half-maximum (fwhm) was determined for these measurements. Knowledge of the instrument function is needed to allow for contamination by lines not fully resolved from adjacent features. This is important for the determination of intensity ratios of emissions from the same upper state. A frequency stabilised laser was used to define the instrument function at 632.82 nm. Two equal intensity functions of the measured laser profile separated by the OH(8–3) $P_1(3)$ Λ-doublet spacing (0.0145 nm) are then best-fitted to an average $P_1(3)$ profile by jointly varying the fwhm of the two laser profiles. The fwhm-adjusted laser profile is the instrument function at the $P_1(3)$ wavelength, $\lambda734.1$ nm.

During 1990, the optical axis of the CTS was aligned 30° above the SE horizon (azimuth 130° E), away from the most aurorally active region of the sky. Spectra were accumulations of five sequential scans, with photon counts in each scan made at 0.1-s integration and 0.005-nm intervals. OH(8–3) and (6–2) P-branch spectra were acquired alternately. For the OH(8–3) band, each spectrum covers $\lambda730$ to $\lambda744.5$ nm and took ~50 min to acquire. For the OH(6–2) band, each spectrum covers $\lambda837.5$ to $\lambda856.0$ nm and took an hour to acquire. The instrument function at OH(8–3) wavelengths
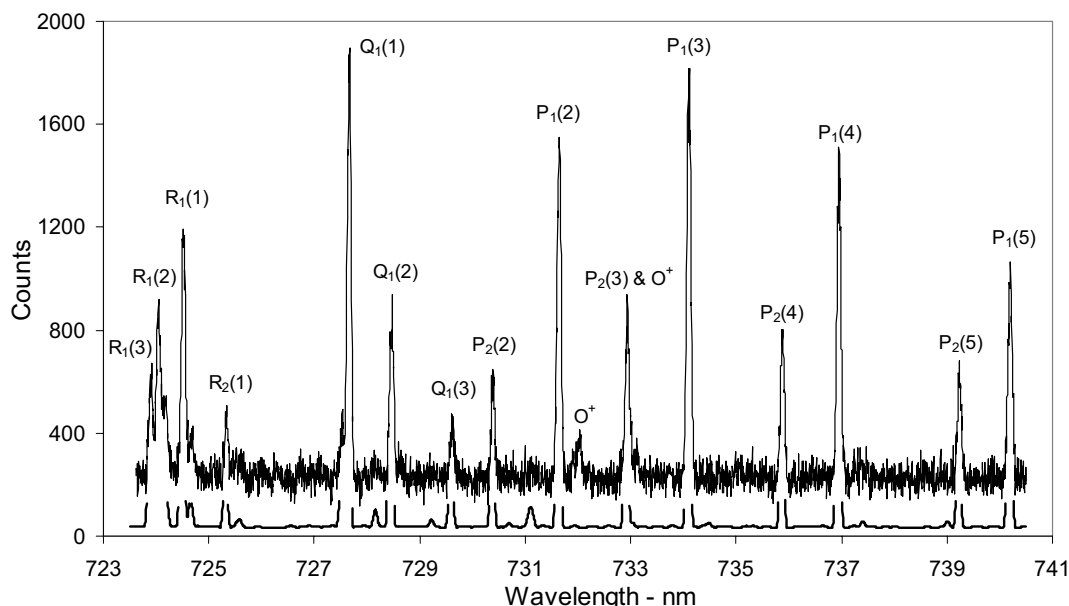
Fig. 1. OH(8–3) hydroxyl airglow (94 summed spectra, clear skies or "thin cloud", Moon below horizon, no aurora apparent). A theoretical spectrum, plotted below the summed spectrum, indicates the expected thermalized hydroxyl airglow contribution to the background.

has a fwhm of ~0.158 nm and at OH(6–2) wavelengths has a fwhm of ~0.154 nm.

In 1990, a calibration lamp was scanned on 9 separate occasions, with 5 scans on each occasion. The lamp was first calibrated against a spectral standard in 1996. It has been assumed that the 1996 calibration measures the spectral shape in 1990 (see Greet et al., 1998). Spectral calibration uncertainties for the 1990 spectra equate to a 2.0 K uncertainty in derived temperatures from both the OH(8–3) and OH(6–2) bands.

The CTS was operated without an appropriate order separation filter during 1990. This does not significantly effect the OH(8–3) spectra, but results in the dominant auroral contamination in the 1990 OH(6–2) spectra being second-order N_2^+ 1Neg (0–1) and (1–2) band emissions. Further details of the 1990 OH(6–2) spectra are presented by Greet et al. (1998), but we adopt a different approach to background removal which is noted later.

A broad classification of sky conditions (clear, thin cloud, patchy cloud, overcast) was maintained through visual observation and (1999 only) reference to an all-sky video system. The "thin cloud" classification describes times of uniform, thin, high cloud, through which bright stars are visible. During cold Antarctic winters at Davis, this is a common sky condition.

When selection against auroral contamination was required, reference was made to wide-angle (60° fov), zenith-oriented photometer measurements of the aurorally activated N_2^+ 1NG band at λ428 nm.

Data acquired during twice-daily balloon flights conducted by the Australian Bureau of Meteorology at Davis were used to determine atmospheric water vapour content.

3 The OH(8–3) spectral region and its contamination

The dominant emissions of the OH(8–3) spectral region are labelled in Fig. 1. The spectrum in Fig. 1 is a summation of 94 of the April 1999 spectra for which the sky conditions were classified as clear or "thin cloud" (hereafter referred to as "clear sky") and no auroral emission was apparent in the wide-angle photometer monitoring the N_2^+ 1NG (0–1) band at λ428 nm. The broad features of the R-, Q- and lower rotational state P-branch structure are apparent.

A theoretical hydroxyl spectrum derived from LWR transition probabilities using a temperature of 214 K, convolved with our instrument function (including the grating Rowland ghosts which are just visible for the most intense lines at the resolution displayed), is presented below at the combined spectrum in Fig. 1. It shows minor OH features at the magnitude they are expected within the background. The temperature used to derive the theoretical spectrum is the "best-fit" value determined from the summed spectrum. Tables 1 and 2 include lists of the wavelengths of the major OH(8–3) lines and weak intensity hydroxyl features in this spectral region, respectively. Adjacent spectral emissions contribute to the intensities at specified wavelengths depending on the instrument function. The wavelength location of the maximum intensity may also be slightly shifted in this manner. To provide the reader with an indication of the relative intensities of significant OH(8–3) emissions, also listed in Table 1 are the expected and measured peak intensities and locations of the major features relative to $P_1(3)$. The relative theoretical peak intensities and locations are determined after convolution with the instrument function. Note that the spectrum compared is the sum of 94 individual spectra of varying temperatures, and these comparisons thus serve only as a

Table 1. The main OH(8–5) branch lines. A theoretical spectrum (LWR, 214 K) has been convolved with the instrument function and the peak wavelength ($\lambda_{\text{peak conv.}}$) and peak intensity ($P_{\text{theory}}$) relative to the $P_1(3)$ emission is listed and compared with measurements from Fig. 1 (λ_{obs} and P_{obs}). Blended lines are indicated by symbols (∗, +, x).

Line	λ_{air} (nm)	$\lambda_{\text{peak conv.}}$ (nm)	λ_{obs} (nm)	P_{Theory} (%)	P_{obs} (%)
$R_1(3)$f	723.88	723.88	723.89	26.3	25.4
e	723.88				
$R_1(2)$f	724.02	724.02	724.03	43.4	42.5
e	724.02				
$R_1(4)$e	724.09 *	724.12	724.13	19.2	19.2
f	724.09 *				
$R_2(3)$e	724.14 *				
f	724.15 *				
$R_2(4)$e	724.19 *				
f	724.20 *				
$R_1(1)$f	724.49 +	724.50	724.51	59.1	58.0
e	724.49 +				
$R_2(2)$e	724.51 +				
f	724.51 +				
$R_1(5)$e	724.65 ×	724.66	724.66	7.6	12.1
f	724.66 ×				
$R_2(5)$e	724.66 ×				
f	724.66 ×				
$R_2(1)$f	725.31	725.32	725.32	16.5	16.2
e	725.32				
$Q_2(1)$e	727.51	727.51	727.52	12.5	16.2
f	727.52				
$Q_1(1)$e	727.64	727.64	727.65	106.1	102.1
f	727.64				
$Q_1(2)$e	728.44	728.45	728.46	43.1	39.4
f	728.45				
$Q_1(3)$e	729.58	729.59	729.61	16.6	14.1
f	729.61				
$P_2(2)$e	730.37	730.38	730.38	25.2	24.9
f	730.38				
$P_1(2)$e	731.62	731.63	731.63	80.6	83.1
f	731.63				
$P_2(3)$e	732.91	732.92		39.9	
f	732.92				
$P_1(3)$	734.08	734.09	734.09	100.0	100.0
f	734.10				
$P_2(4)$e	735.87	735.87	735.87	36.7	36.1
f	735.87				
$P_1(4)$e	736.93	736.94	736.95	82.2	75.2
f	736.95				
$P_2(5)$f	739.22	739.22	739.22	26.2	27.0
e	739.22				
$P_1(5)$e	740.17	740.19	740.19	49.2	50.6
f	740.20				

Table 2. OH(8–3) background features and unthermalised OH emissions. A theoretical spectrum (LWR, 214 K) has been convolved with the instrument function and the peak wavelength ($\lambda_{\text{peak conv.}}$) and peak intensity ($P_{\text{theory}}$) relative to the $P_1(3)$ emission is listed for the thermalised components. Blended lines are indicated by a symbol (∗).

Line	λ_{air} (nm)	$\lambda_{\text{peak conv.}}$ (nm)	P_{Theory} (%)
$R_2(6)$e	725.53 *	725.58	1.8
f	725.53 *		
$R_1(6)$e	725.58 *		
f	725.60 *		
$Q_2(2)$e	728.15	728.16	4.2
f	728.17		
(7-2) $P_2(12)$f	728.57	729.22	1.8
e	728.65		
(7-2) $P_1(12)$e	728.97		
f	729.11		
$Q_2(3)$e	729.21		
f	729.23		
$Q_2(4)$e	730.69	730.69	1.0
f	730.70		
$Q_1(4)$e	731.08	731.11	5.1
f	731.13		
$^Q R_{12}(1)$e	734.49	734.49	1.1
f	734.49		
(7-2) $P_2(13)$f	734.69		
e	734.79		
(7-2) $P_1(13)$e	735.06		
f	735.21		
$^P Q_{12}(2)$e	737.40	737.41	1.4
f	737.41		
$^P Q_{12}(3)$e	739.00	739.01	1.4
f	739.02		

guide. Goldman (1982) derives satellite line (see Appendix) transition probabilities consistent with Mies transition probabilities of the main branch transitions. In order to estimate the satellite line intensities equivalently for LWR transition probabilities, we have scaled the Goldman (1982) values in the same ratio to the appropriate P-branch transition proba-

bility. These are used to calculate the satellite line theoretical values provided, along with those for other weak-intensity, thermalised hydroxyl emissions in Table 2.

At some level of J', the hydroxyl rotation state populations become non-thermal (see, e.g. Pendleton et al., 1993). States of high J' may have wavelengths sufficiently different from the dominant band lines, to extend into another band. Measured intensities, while low relative to the major P-branch lines (at most a few %), may be several orders of magnitude larger than the theoretical thermalised intensities (Pendleton et al., 1993). While of low intensity, these emissions may contaminate major lines or background regions in a systematic manner. Greet et al. (1998) noted and demonstrated that unthermalised OH(5–1) $P_1(12)$ emissions are blended with OH(6–2) $P_1(3)$, rendering this major line suspect for rotational temperature determinations. Osterbrock et al. (1996) using spectra from the high resolution (∼0.02 nm) echelle
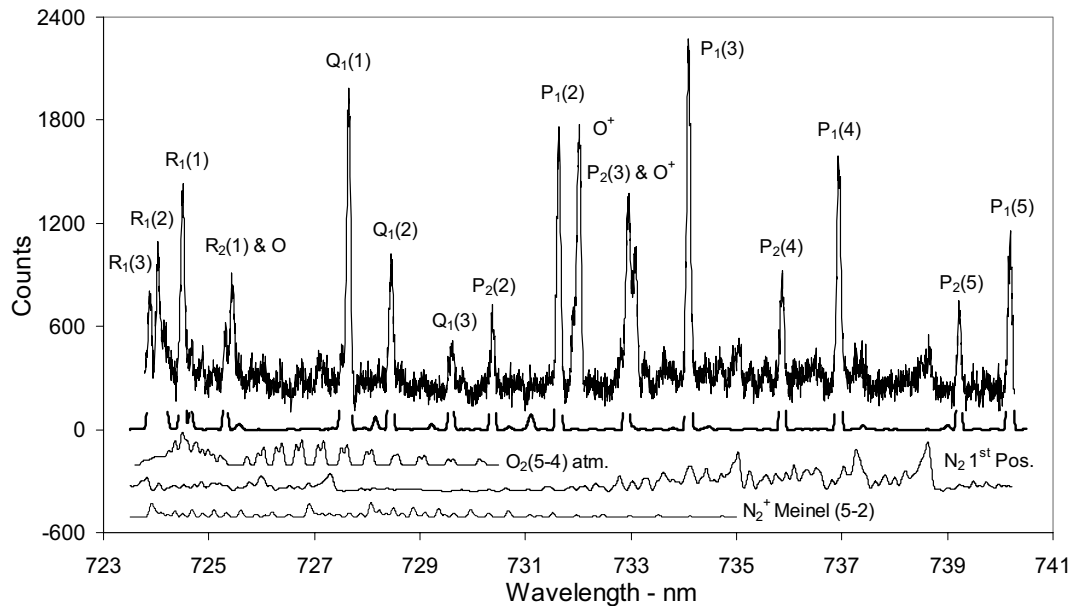
Fig. 2. Auroral contamination (116 summed spectra, Moon below horizon, aurora apparent). A theoretical hydroxyl and O_2(5–4) Atmospheric, N_2 1st Positive and N_2^+ Meinel (5–2) theoretical auroral spectra are shown below the summed spectrum.

spectrograph on the Keck 10-metre telescope at Mauna Kea, lists the unthermalised OH emissions that extend into the OH(8–3) spectral region. The wavelength of these OH(7–2) emissions are also listed in Table 2. On the long wavelength side of Q_1(2) in Fig. 1 is an unassigned feature that could be mistaken for unthermalised OH(7–2) P_2(12). We consider this association unlikely, because OH(7–2) P_1(12), which should be of similar intensity, is not as readily apparent in the spectrum. We can make no definitive assignment for the feature noted.

Despite our efforts, some high-altitude dayglow or weak auroral features are apparent in Fig. 1. The $O^+(^2P^o_{1/2} \rightarrow {}^2D^o_{5/2})$ emission at $\lambda731.92$ nm and the more intense $O^+(^2P^o_{3/2} \rightarrow {}^2D^o_{5/2})$ emission at $\lambda732.02$ nm are merged at our instrument resolution but separated from P_1(2) at $\lambda731.63$ nm. Values derived from our spectra are used for these wavelengths (see later in this section), but the "air" wavelengths listed in the Atomic Line List (www.pa.uky.edu/~peter/atomic/) are used for other atomic and ionic emissions. Further O^+ emissions at $\lambda732.97$ nm $(^2P^o_{1/2} \rightarrow {}^2D^o_{3/2})$ and at $\lambda733.07$ nm $(^2P^o_{3/2} \rightarrow {}^2D^o_{3/2})$ are blended with P_2(3) at $\lambda732.92$ nm. These O^+ lines result from a metastable state with a theoretical radiative lifetime of ~5 s (Smith et al., 1982). The upper state is activated by low energy auroral electrons or sunlight. Collisional deactivation limits intense O^+ emissions at $\lambda732$ nm and $\lambda733$ nm to altitudes above 200 km (Rusch et al., 1977; Smith et al., 1982). The high altitude of these ionic emissions means they can still be activated by sunlight after the hydroxyl layer at ~87 km is in darkness. For this reason, specific care must be taken when deriving rotational temperatures using low-resolution (fwhm>~0.16 nm) measurements of the OH(8–3) P_1(2) line which may be contaminated by dayglow O^+ emis-

sions collected when the Sun is illuminating the atmosphere at ~300 km (solar elevation >−17° for zenith observations).

N_2 1st Positive (6–4), (5–3), (4–2), N_2^+ Meinel (5–2) and $O_2(b^1\Sigma_g^+ - X^3\Sigma_g)$(5–4) bands potentially contaminate the OH(8–3) band. Figure 2 is a summation of 116 spectra collected when optical aurora is apparent on the wide-angle photometer monitoring the N_2^+ 1NG (0–1) band at $\lambda428$ nm and the Moon is below the horizon. The O^+ emissions near $\lambda732$ nm and those blended with P_2(3) near $\lambda733$ nm are significantly more intense relative to the OH features in Fig. 2 than in Fig. 1, indicating an auroral contribution to their intensity. An atomic oxygen triplet near $\lambda725.44$ nm, from the transitions $^3S^o_1 \rightarrow {}^3P_{0,1,2}$, is also readily apparent. The intensity of the atomic and ionic auroral emissions in Fig. 2, relative to the OH(8–3) P_1(3) intensity, are listed in Table 3.

To assist with the determination of auroral band features in this spectral region, theoretical spectra of the O_2 (5–4) atmospheric, the N_2^+ Meinel (5–2) and the summed N_2 1st Positive bands [(5–3), (6–4) and (4–2)] have been convolved with the instrument function and separately displayed below the combined, measured spectra in Fig. 2. The N_2 1st Positive (3–1) and (7–5) and N_2^+ Meinel (6–3) bands do not extend into the OH(8–3) spectral range considered, and the N_2^+ Meinel (4–1) band contributes less than 3% of the auroral contamination at any wavelength in the OH(8–3) spectral range considered. Programs for generating synthetic auroral spectra of the nitrogen bands were obtained by private communication (Gattinger; see also Gattinger and Vallance Jones, 1974). A temperature of 300 K is used for the theoretical nitrogen aurora spectra.

The N_2 1st Positive (5–3) band is the dominant auroral contaminant in the interval from $\lambda733$ nm to $\lambda739$ nm. The
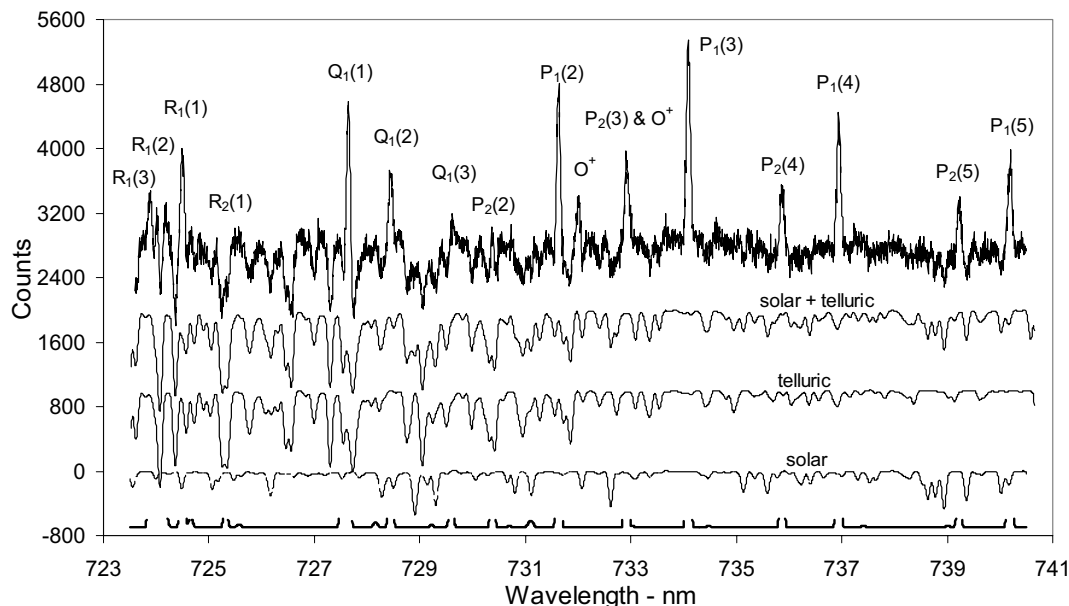
Fig. 3. Scattered moonlight influence (126 summed spectra, scattered moonlight, no aurora apparent). The Kitt Peak solar and telluric spectra, both combined and separately, and a theoretical hydroxyl spectrum are shown below the summed spectrum.

Table 3. Airglow and auroral, atomic and ionic lines and molecular bands in the OH(8–3) region, their wavelength of peak intensity within the interval $\lambda 723$ nm to $\lambda 741$ nm and their intensity relative to OH(8–3) $P_1(3)$ (scaled from Fig. 2).

Auroral feature	λ_{air}(nm)	%P_1(3)
(a) atomic & ionic auroral lines		
O ($^3S^o_1 \rightarrow {}^3P_{0,1,2}$)	725.44	32
O$^+$ ($^2P^o_{1/2} \rightarrow {}^2D^o_{5/2}$)	731.92	22
O$^+$ ($^2P^o_{3/2} \rightarrow {}^2D^o_{5/2}$)	732.02	77
O$^+$ ($^2P^o_{1/2} \rightarrow {}^2D^o_{3/2}$)	732.97	36
O$^+$ ($^2P^o_{3/2} \rightarrow {}^2D^o_{3/2}$)	733.07	39
(b) auroral bands (λ peak in region)		
O$_2$ b-X Atm (5-4)	724.50	9.9
N$_2$ 1st Pos (6-4)	727.30	5.3
N$_2^+$ Meinel (5-2)	728.07	4.5
N$_2$ 1st Pos (5-3)	738.63	15
N$_2$ 1st Pos (4-2)	739.99	0.004

N$_2$ 1st Positive theoretical spectrum has been matched to the combined, measured spectra by minimising the least-square residuals to selected portions within this region of the spectrum. This "best-fit" theoretical spectrum is used to set the intensity for theoretical calculations of all nitrogen aurora in this region, including the N$_2^+$ Meinel (5–2) band. The peak intensities and associated wavelength of each of the auroral N$_2$ 1st Positive bands and the N$_2^+$ Meinel (5–2) band in Fig. 2, as determined from the theoretical spectra, are listed in Table 3. These values, which are listed relative to the peak P$_1$(3)

intensity, depend on the intensity of the aurora but provide an indication of the relative importance of the auroral bands in the OH(8–3) spectral region for average auroral conditions at Davis (magnetic latitude 74.6° S). When viewing Table 3, please note that the N$_2$ 1st Positive (4–2) band is more intense at longer wavelengths than within the OH (8–3) spectral region considered.

The O$_2$ b-X Atmospheric (5–4) band is the most significant auroral band contaminant in the R- and Q-branch regions, although the N$_2$ 1st Positive (6–4) and N$_2^+$ Meinel (5–2) bands also contribute. Slanger et al. (1997) have reported detection of O$_2$ Atmospheric (5–4) nightglow using the Keck/HIRES spectra from Mauna Kea. The peak intensities of the O$_2$ b-X Atmospheric (5–4) nightglow lines are more than two orders of magnitude less intense than the brightest OH(8–3) emissions (Slanger et al., 2000) but can be significantly enhanced during aurora (Gattinger and Vallance Jones, 1976). We have used the theoretical spectrum of the O$_2$ b-X Atmospheric (5–4) band published by Slanger and Osterbrock (1998), convolved with our instrument function, and minimised the least-square residuals of fitting it to a region between the R-and Q-branches. The theoretically determined N$_2$ 1st Positive (6–4) and N$_2^+$ Meinel (6–2) band contributions were subtracted before the O$_2$ b-X Atmospheric (5–4) contribution was determined. Measured in this manner, the peak intensity of the O$_2$ b-X Atmospheric (5–4) band relative to the P$_1$(3) emission is $\sim$10% (see Table 3), strongly indicating auroral enhancement of this band.

The "air" wavelengths listed in the Atomic Line List for O$^+$($^2P^o_{3/2} \rightarrow {}^2D^o_{5/2}$) and O$^+$($^2P^o_{1/2} \rightarrow {}^2D^o_{5/2}$) are $\lambda 732.00$ nm and $\lambda 731.89$ nm, respectively. A least-squares best-fit of the CTS instrument function to this region of Fig. 2 yields wavelengths of $\lambda 732.02$ nm and $\lambda 731.915$ nm

and a relative intensity of 1:0.28. Smith et al. (1982), who observed this region with a Fabry-Perot spectrometer, use a wavelength of $\lambda 732.02$ nm for the $O^+(^2P^o_{3/2} \rightarrow ^2D^o_{5/2})$ emission. This value is consistent with our measurement. However, Smith et al. (1982) list in their Abstract a separation of 0.08 nm for these O^+ lines. This may not be a value that they have measured, and it is not supported by our measurements, which indicate a separation of 0.105 ± 0.005 nm.

Scattered sunlight may influence spectra collected at low solar depression angles or when moonlight and cloud are present. The spectrum in Fig. 3 is a summation of 126 spectra collected when scattered moonlight could enter the field-of-view of the instrument and no auroral activity is apparent. Below this are presented, both combined and separately, solar and telluric spectra determined from Kitt Peak spectra at varying solar zenith angles (Wallace et al., 1998), convolved with the CTS instrument function. Both solar and atmospheric absorption lines are clearly visible in the CTS spectrum, and collectively account for the absorption features in the spectrum. Comparison with HITRAN data (Rothman et al, 1998, 2003; www.HITRAN.com) indicates water vapour is the only significant atmospheric absorber in this wavelength region.

Figures 4a, b and c show expanded portions of the combined solar and telluric, high-resolution Kitt Peak spectrum in the vicinity of the $Q_1(1)$, $P_1(4)$ and $P_1(5)$ emissions and the Doppler-broadened, lamda-doubled, OH emission lines (after Espy and Hammond, 1995). The average winter water vapour content above Davis in 1999, derived from twice-daily meteorological balloon flights, is 2.3 mm (7.695 E+22 molecules cm^{-2}). Also shown in Figs. 4 a, b and c, are the pressure-broadened, absorption profiles for typical Davis winter conditions, based on HITRAN 2001 line parameters. For average Davis winter conditions, we calculate that 3.1% of OH(8–3) $Q_1(1)$ and 2.3% of OH(8–3) $P_1(4)$ are absorbed. Other OH(8–3) lines of interest with measurable absorption are $R_1(2)$ and $R_1(1)$. These are, respectively, 1.2% and 0.6% absorbed. A table of atmospheric absorption of the major OH(8–3) lines for a range of atmospheric conditions printed in Espy and Hammond (1995) is unfortunately a printing error, being a repeat of the OH(6–2) Table. The actual values calculated for that paper are comparable with our estimates (Espy, private communication). The absorption by water vapour for the lines noted will be significantly exacerbated at lower latitude sites, which typically have much wetter atmospheres. Espy and Hammond (1995) use 29, 21, 8.5 and 4.2 mm of H_2O as typical mid-latitude summer, high-latitude summer, mid-latitude winter and high-latitude winter atmospheric water vapour content estimates.

Typically P-branch hydroxyl lines are used to derive rotational temperatures. In order to quantify the effect of atmospheric water vapour on temperatures derived using the OH(8–3) $P_1(4)$ emission, consider a relatively dry atmosphere containing 5 mm of water vapour. Zenith measurements of the $P_1(4)$ intensity would be reduced by $\sim$5% and temperatures derived using LWR transition probabilities from the $P_1(2)/P_1(4)$ intensity ratio would be reduced
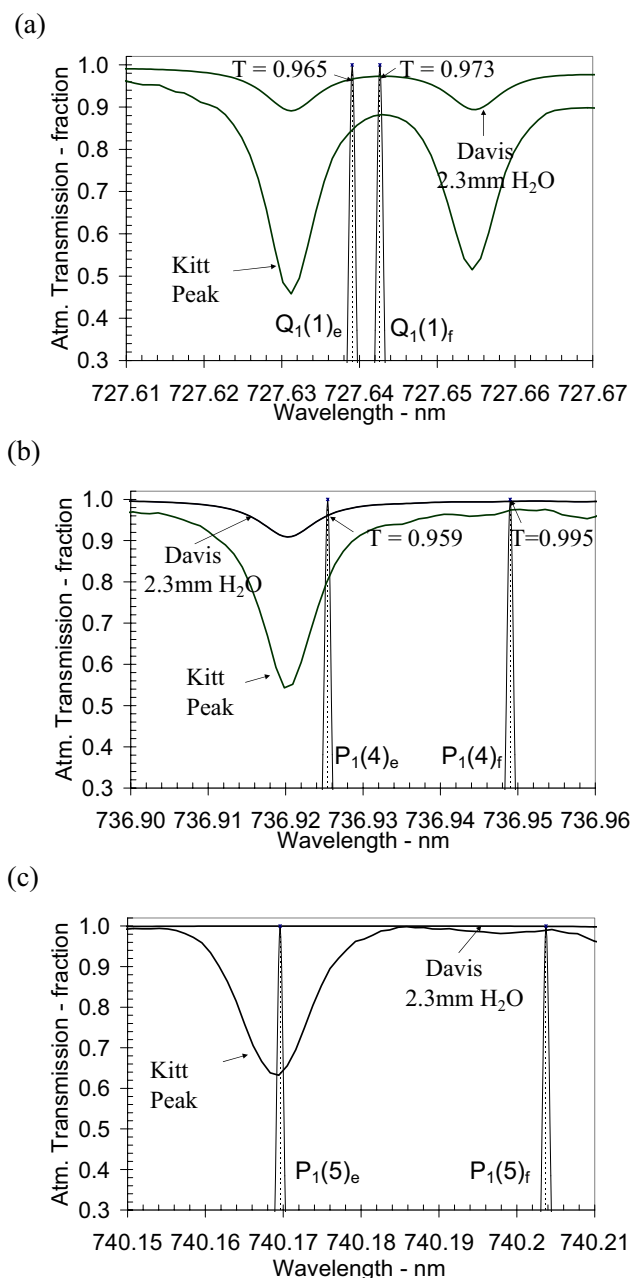

Fig. 4. An expansion of the OH(8–3) $Q_1(1)$, $P_1(4)$ and $P_1(5)$ spectral regions, showing the Kitt Peak combined solar and telluric, high-resolution spectrum and a pressure-broadened, water vapour spectrum for typical Davis winter conditions (2.3 mm H_2O, HITRAN 2001 line parameters). The hydroxyl line e and f components are shown with appropriate Doppler broadening (after Espy and Hammond, 1995).

by $\sim$10 K, from the $P_1(3)/P_1(4)$ ratio would be reduced by $\sim$17 K and from the $P_1(4)/P_1(5)$ ratio would be increased by $\sim$15 K. The magnitude of these errors is dependent on the highly variable atmospheric water vapour content.

Osterbrock et al. (1997) briefly address the issue of atmospheric absorption of the hydroxyl airglow lines observed by the Keck telescope on Mauna Kea (altitude $\sim$4200 m).

Table 4. OH(8–3) temperature-insensitive intensity ratios derived from T&L, Mies and LWR transition probabilities and values determined from the summed high-resolution spectrum in Fig. 1.

Ratio	T&L	Mies	LWR	Expt.
$Q_1(1)/P_1(2)$	1.44	1.35	1.31	1.22 ± 0.03
$Q_1(2)/P_1(3)$	0.50	0.45	0.43	0.40 ± 0.02
$Q_1(3)/P_1(4)$	0.25	0.22	0.21	0.18 ± 0.02
$R_1(1)/P_1(3)$	0.55	0.47	0.43	0.44 ± 0.03
$R_1(2)/P_1(4)$	0.69	0.56	0.49	0.47 ± 0.02
$R_1(3)/P_1(5)$	0.75	0.58	0.48	0.44 ± 0.03

They discuss the OH(8–3) $P_1(4)_e$ line and its proximity to a water vapour absorption line, but conclude that absorption did not appear to be significant. The pressure broadening of the water vapour lines is significantly less at the altitude of Mauna Kea ($\sim$0.006 nm) compared to sea-level ($\sim$0.008 nm), thus absorption may be significantly reduced for the Mauna Kea site compared with Davis. On-going research utilizing Mauna Kea observations (Cosby, private communication) supports the possibility of measurable atmospheric absorption of the OH(8–3) $P_1(4)$ emission even for this high-altitude observatory.

Figure 4c shows an expansion of the $P_1(5)$ wavelength region. $P_1(5)$ lies close to a solar absorption line. If scattered moonlight enters an instrument's field-of-view, this solar line can potentially be a source of error in determining the intensity of $P_1(5)$, thus influencing derived temperatures.

4 Temperature-insensitive OH(8–3) intensity ratios

Hydroxyl emissions from the same upper rotation-vibration state maintain the same intensity ratio independent of temperature. Temperature-independent intensity ratios are determined from the high-resolution summed spectrum in Fig. 1. The 94 spectra contributing to Fig. 1 were collected when the Moon was below the horizon and auroral contamination was negligible. The analysis is similar to that presented by French et al. (2000) for the OH(6–2) region. Photon counts are determined in wavelength regions, centred on emissions of interest. The width of the "count-region" for $P_1(2)$, $P_1(3)$, $P_1(4)$, $Q_1(1)$, $Q_1(2)$, $R_1(1)$ and $R_1(3)$ is 0.155 nm. A count-region of 0.135 nm is used for $P_1(5)$, $Q_1(3)$ and $R_1(2)$. The percentage of the emission of interest contained in the count region, and from "blended" emissions, is determined by reference to the instrument function.

For the spectra contributing to Fig. 1, the average water vapour content determined from the balloon flights on those days was 1.7 mm. The HITRAN 2001 line parameters were used to calculate and to allow for the absorption by this amount of water vapour on the measured OH(8–3)

$Q_1(1)$, $P_1(4)$, $R_1(1)$ and $R_1(2)$ intensities. The contribution of unresolved hydroxyl emissions to the count region is calculated from the instrument function and LWR transmission probabilities at a temperature of 214 K. Error estimates of these contaminations are calculated as the difference obtained using LWR transition probabilities at temperatures of 200 K and 230 K. A total uncertainty for each intensity measurement is determined by adding in quadrature errors from counting statistics, in estimating the background level, and uncertainties in calculating the contribution of contaminating emissions. The most difficult line intensities to estimate are $R_1(1)$, $R_1(2)$ and $R_1(3)$. $R_1(1)$ is significantly blended with $R_2(2)$, with minor contributions from $R_1(5)$ and $R_2(5)$. 28.2% of the signal under the $R_1(1)$ count region is contributed by other hydroxyl emissions. $R_1(2)$ is significantly blended with $R_1(4)$, which is itself significantly absorbed by water vapour (20.0% for 1.7 mm H_2O), with minor contributions from $R_2(3)$ and $R_1(3)$. 13.0% of the signal under the $R_1(2)$ count region is contributed by other hydroxyl emissions. The $R_1(3)$ count region is contaminated by $R_1(2)$, which contributes 6.0% of the measured signal. The count regions for other emissions contain less than a 1% contribution from blended hydroxyl emissions.

The OH(8–3) temperature-insensitive intensity ratios determined from the summed 1999 spectrum, along with the corresponding values from Mies, T&L and LWR, are detailed in Table 4. The experimentally determined Q/P ratios are lower than the values determined from the published transition probabilities, although the LWR ratios are closest. Of the LWR Q/P ratios, only $Q_1(1)/P_1(2)$ is significantly different from the measured values, being higher by $\sim$7%. The experimental R/P ratios are significantly lower than the T&L and Mies values but within the measurement uncertainty of the LWR values. The LWR transition probabilities are thus most consistent with temperature-insensitive intensity ratios measured for the OH(8–3) band. French et al. (2000) reported that LWR transition probabilities were most consistent with the temperature-insensitive intensity ratios in the OH(6–2) band. Therefore, it is appropriate to use LWR transition probabilities when comparing OH(8–3) and OH(6–2) hydroxyl rotational temperatures. No implication can be drawn from our experimental measurements of the relative merit of the absolute values of the published transition probabilities, or of the accuracy of the relative differences between vibrational bands (see, for example, Melo et al., 1997).

5 Comparison of OH(6–2) and OH(8–3) winter temperatures

Rotational temperatures were determined from OH(6–2) and (8–3) spectra collected in 1990, using LWR transition probabilities. The intensities of the $P_1(2)$, $P_1(3)$, $P_1(4)$ and $P_1(5)$ emissions were calculated from 0.255-nm wide count regions centred on each emission, with an allowance made for the instrument function and lambda doubling of the lines (as per Greet et al., 1998). Background regions were chosen
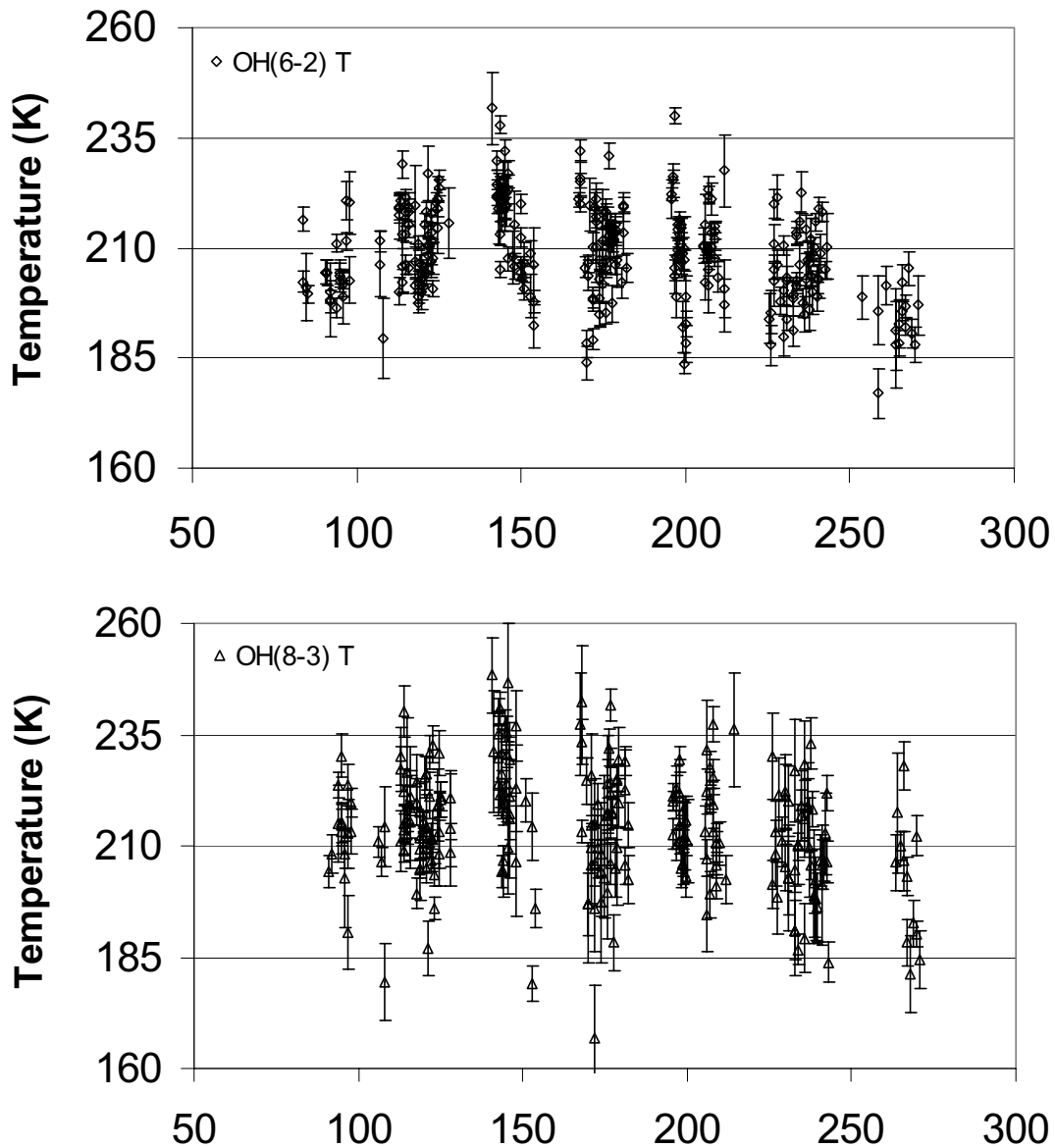
Fig. 5. OH(6–2) and OH(8–3) rotational temperatures determined from spectra collected at Davis in 1990, with ± one sigma errors.

individually for each emission to match minor auroral and scattered moonlight contaminations, for the instrument function used. Temperatures were calculated for each possible ratio. For the OH(6–2) band, a weighted mean temperature is determined after neglecting those ratios involving the $P_1(3)$ emission as this line is blended with the unthermalised OH(5–1) $P_1(12)$ emission (Greet et al., 1998). For the OH(8–3) band, a weighted mean temperature was determined after ignoring those ratios involving the $P_1(4)$ emission. As has been demonstrated in this paper, measured OH(8–3) $P_1(4)$ intensities vary depending on the atmospheric water vapour content. Figure 5 shows the measured OH(6–2) and OH(8–3) temperatures and associated one-sigma errors. Average errors for individual spectra are 4 K and 6 K for OH(6–2) and (8–3), respectively. The OH(8–3) errors are generally larger because of the lower intensity of this emission.

Table 5 shows a comparison of OH(8–3) and (6–2) average temperatures for the winter interval ($106 \leq$ day-of-year ≤ 258; Burns et al., 2002) for "any sky" and "no Moon and clear sky" conditions. Standard errors are listed for the weighted-average temperatures. In 1990, spectra were collected in the two-week intervals centred on "new Moon". Only $\sim$20% of the "any sky" data are collected with the Moon above the horizon. Excluding these data varies the weighted-average temperatures by no more than 0.4 K. More OH(6–2) spectra were available for analysis, and this is noted in Table 5. This may result in a bias, so a separate comparison using only the temperatures from alternate spectra was made. There are 80 alternate OH(6–2) and OH(8–3) temperature measurements from "no Moon and clear" spectra. The average temperature difference is 2.6 K and the standard error is 1.2 K, with OH(8–3) temperatures being warmer. For "any sky"

Table 5. Average hydroxyl rotational temperatures for individual line ratios in the OH(8–3) and OH(6–2) bands over the 1990 winter (106≤day-of-year≤258), separately presented for "no Moon and clear sky" and "any sky" conditions. Standard errors are listed for the "weighted average" temperatures.

Ratio	No moon & Clear Sky		Any Sky	
	OH(6-2) T (# = 111, K)	OH(8-3) T (# = 91, K)	OH(6-2) T (# = 247, K)	OH(8-3) T (# = 216, K)
$P_1(2)/P_1(3)$	214.4	213.0	212.5	216.2
$P_1(2)/P_1(4)$	210.6	197.1	209.8	193.8
$P_1(2)/P_1(5)$	211.0	214.6	210.3	215.1
$P_1(3)/P_1(4)$	208.6	188.9	208.8	183.4
$P_1(3)/P_1(5)$	210.1	215.7	210.0	216.0
$P_1(4)/P_1(5)$	211.9	246.5	211.4	262.0
Wtd. Ave.	210.8±0.9	214.4±1.2	210.1±0.7	214.6±0.9

conditions, there are 227 alternate spectra measurements. For these, the mean difference is 3.9 K and the standard error is 0.8 K, with the OH(8–3) temperatures again being warmer. After including the results from Table 5, the average temperature differences range from 2.6 K to 4.5 K. All are significant at twice the standard error, however, there are sufficient sources of systematic error that could account for differences of these magnitudes. Combining the spectral calibration errors for each band in 1990 in quadrature yields a relative temperature uncertainty of 2.8 K. The measured differences are all within twice this uncertainty.

The influence of water vapour absorption on the OH(8–3) $P_1(4)$ line ratio temperatures is readily apparent in Table 5. The result is similar for temperatures determined from the 1999 clear-sky, summed spectrum. To determine the impact of absorption on the $P_1(4)$ emission, the average intensity of the $P_1(4)$ emission for each of these data sets is increased until the temperature returned from $P_1(4)$ ratios equals the temperatures derived from the other rotational lines. A similar, more rigorous, method was used by Turnbull and Lowe (1983) to calculate atmospheric water vapour content. For the 1999 clear-sky spectrum (zenith viewing, air mass 1), we estimate 4.5% of $P_1(4)$ emission has been absorbed. For the 1990 spectra (60° off-zenith viewing, air mass 2) 7.4% of $P_1(4)$ for the clear-sky spectrum and 8.9% for the any sky spectrum has been absorbed. Taking into account the factor of two in the atmospheric path-length between the 1990 and 1999 spectra, and the expected increase in water vapour between "no Moon and clear" and "any sky" conditions, the agreement between these results is reasonable. From HITRAN 2001 line parameters, this equates to an atmospheric water content of 5.0 mm for the 1999 spectrum, and 4.1 mm and 4.9 mm for the 1990 clear-sky and any sky spectra. This is high compared with 1.7 mm water vapour

content for the 1999 spectrum and 2.3 mm for the average Davis winter value, estimated from the meteorological data. The water vapour content estimated from the reduction in the OH(8–3) $P_1(4)$ intensity and HITRAN line parameters is thus ∼2.5 times greater than measured by the meteorological balloons at Davis.

Several assumptions have been made in the estimate of the absorption, but the errors introduced are expected to be small. The Λ-doubled components of the $P_1(4)$ emission are assumed to be of equal intensity, with absorption of the rotational line calculated as an average of the individual absorptions. Osterbrock et al. (1997) measures the intensity of individual Λ-doubled components and reports that the OH(8–3) $P_1(4)_e$ line is 4% more intense than OH(8–3) $P_1(4)_f$. The OH(8–3) $P_1(4)_e$ line is the component subjected to greater absorption by water vapour (see Fig. 4b). If the OH(8–3) $P_1(4)_e$ line were actually 10% brighter than its companion, our water vapour estimates would be high by only ∼8%. Errors in HITRAN 2001 line intensities for water are only expected to be of the order of a few percent.

Another source of error may be uncertainties in the LWR transition probabilities. Repeating the calculation for the 1999 spectrum using the Mies transitional probabilities, the estimated absorption is similar (4.3%). A recent comparison of radiosonde and satellite measurements, Wang et al. (2002), suggests meteorological balloon data may underestimate the atmospheric water vapour content. Applying the suggested correction indicates an underestimation of the Davis winter water vapour content measurements by only ∼7%. Some H_2O in the atmosphere above Davis in winter may be missed by meteorological balloon measurements when it is in the ice-phase, and the absorption parameters for ice may differ from water vapour. The reason for the discrepancy may lie in one or a combination of these factors, which we cannot yet quantify.

6 Conclusions

Measurements of the OH(8–3) temperature-independent Q/P and R/P line ratios are generally consistent with LWR transition probabilities, and lower than Mies and T&L transition probabilities. This is broadly consistent with measurements reported by French et al. (2000) for the OH(6–2) band, and provides additional support for those results. Of the LWR ratios in the OH(8–3) band, only $Q_1(1)/P_1(2)$ is significantly different from the measured values, being higher by ∼7%. For the transition probabilities considered, which yield an ∼18 K variation in derived temperature, the LWR values are the most appropriate for determining rotational temperatures from OH(8–3) measurements.

The location of $O^+(^2P^o_{3/2} \rightarrow {}^2D^o_{5/2})$ and $O^+(^2P^o_{1/2} \rightarrow {}^2D^o_{5/2})$ has been determined to be $\lambda732.02$ nm and $\lambda731.915$ nm, respectively, and their relative auroral intensity to be 1:0.28. There is some inaccurate information in the literature about the location of these lines. These ionic emissions are also activated by sunlight. Care must

be taken when deriving rotational temperatures involving OH(8–3) $P_1(2)$ at $\lambda731.63$ nm, that either the observing instrumentation has sufficient spectral resolution to fully resolve this emission (fwhm<~0.16 nm) from the O^+ lines, or that the Sun is no longer illuminating the atmosphere at ~300 km (solar elevation $<-17°$ for zenith observations) and auroral activity is negligible. If not correctly accounted for, the influence on derived temperatures depends strongly on the degree to which OH(8–3) $P_1(2)$ is overestimated due to contamination by the O^+ lines. Overestimation of the $P_1(2)$ intensity results in calculation of a reduced rotational temperature. Contamination of the $P_1(2)$ intensity by O^+ emissions would typically result in an erroneously determined temperature increase through the early evening as the O^+ dayglow faded.

Water vapour absorption of OH(8–3) $P_1(4)$, ~1% for 1 mm of water vapour (3.346E+21 molecules cm^{-2}), is of significant concern for temperature derivations from this band despite some published information unfortunately suggesting that this is not the case. For a relatively dry atmosphere containing 5 mm of water vapour, temperatures derived from zenith measurements of the $P_1(2)/P_1(4)$ intensity ratio would be reduced by ~10 K, from the $P_1(3)/P_1(4)$ ratio would be reduced by ~17 K and from the $P_1(4)/P_1(5)$ ratio would be increased by ~15 K. The magnitude of these errors is dependent on the highly variable atmospheric water vapour content and would distort night-to-night and seasonal temperature variations.

We cannot resolve a discrepancy of ~2.7 between the estimated $P_1(4)$ absorption from airglow measurements and the combination of the HITRAN 2001 line parameters and Davis meteorological balloon measurements of water vapour.

The relative intensities of the major auroral contaminants of the OH(8–3) band at Davis have been determined. The major auroral contaminant of the P-branch lines is the N_2 1st Positive (5–3) band.

$P_1(5)$ lies close to a solar absorption line. If scattered moonlight enters an instrument's field-of-view, this solar line can be a source of error in determining the intensity of $P_1(5)$ and thus for the use of this line in determining rotational temperatures.

For consecutive measurements of OH(8–3) and OH(6–2) spectra at Davis in 1990, we determine a difference of ~4 K in rotational temperatures, with the OH(8–3) derived temperatures being warmer. This may be due to transition probability uncertainties or inaccuracies in our spectral calibrations. It also demonstrates a difficulty in melding hydroxyl temperatures derived from different hydroxyl bands when determining climate trends.

Appendix A

A short summary of the nomenclature used in this paper to describe hydroxyl airglow emissions is presented here to assist readers.

The hydroxyl ground state is spin-orbit degenerate into $X^2\Pi_{3/2}$ and $X^2\Pi_{1/2}$ states with total angular momentum $J=1.5$ and 0.5 respectively. Orbital angular momentum, L, of positive integer value can be added, thus, the $X^2\Pi_{3/2}$ state can be labelled with $J=0.5, 1.5, 2.5,...$, and the $X^2\Pi_{1/2}$ state can be labelled with $J=0.5, 1.5, 2.5,...$. Alternatively, the rotational states can be labelled by the orbital angular momentum, where $L=J-1/2$ for the $X^2\Pi_{3/2}$ state and $L=J+1/2$ for the $X^2\Pi_{1/2}$ state. We label hydroxyl transitions

$$OH(v'-v'')^{\Delta L}\Delta J_{s's''}(L'')_{\Lambda''}.$$

In this nomenclature, v is the vibrational quantum number, L and J are as described above, s is the spin quantum number, Λ is the Λ-doubling designator and ' and '' indicate upper or lower state values, respectively.

For transitions within the spin-orbit degenerate ground states, $s'=s''$ and $\Delta L=\Delta J$, then the redundant s'' and ΔL are dropped. Transitions between the spin-orbit degenerate ground states are known as satellite transitions and have intensities of at most, a few percent of the brightest branch lines.

ΔJ is limited by a quantum selection rule to -1, 0 or 1 and is given a letter label which denotes the P-, Q- and R-branches, respectively. ΔL can have values -2, -1, 0, 1 or 2 and is represented by an expanded lettering system as O, P, Q, R or S. The spin quantum number is either 1 or 2. Transitions within the lower potential spin-orbit degenerate ground state, $X^2\Pi_{3/2}$, are designated by the 1 subscript and are approximately three times as bright as the equivalent transitions within the higher potential spin-orbit degenerate ground state, $X^2\Pi_{1/2}$, which is designated by the 2 subscript.

Each rotational state is further split (Λ-doubled) due to nuclear-spin, electron-orbit interactions. Transitions are distinguished by letter subscripts e or f, indicating the parity of the lower state. The Λ-doubled components are spectrally close, but the separation increases with L''. Our CTS typically cannot resolve the Λ-doubled components but the varying separation of Λ-doubled components within rotational lines must be allowed for with the methods we use, for determining line peaks and total intensities. For the purpose of the point being made, if there is no need to distinguish between the Λ-doubled components, then the Λ'' subscript (e or f) is often dropped.

The ΔJ quantum selection rule means that an upper rotational state, within a specified vibrational band transition, may emit via three possible transitions within its spin-orbit degenerate ground state (the associated P- Q- and R-branch lines) or via three weak transitions between the spin-orbit degenerate ground states (the associated satellite lines). It is the relative proportions emitted via these possible transitions that are allowed for by the transition probabilities, A_a and A_b, in Eq. (1).

References

Akmaev, R. A. and Fomichev, V. I.: Cooling of the mesosphere and lower thermosphere due to doubling of CO_2, Ann. Geophys., 16, 1501–1512, 1998.

Akmaev, R. A. and Fomichev, V. I.: A model estimate of cooling in the mesosphere and lower thermosphere due to the CO_2 increase over the last 3–4 decades, Geophys. Res. Lett., 27, 2113–2116, 2000.

Baker, D. J. and Stair, A. T.: Rocket measurements of the altitude distributions of the hydroxyl airglow, Phys. Scr., 37, 611–622, 1988.

Berger, U. and Dameris, M.: Cooling of the upper atmosphere due to CO_2 increases: a model study, Ann. Geophys., 11, 809–819, 1993.

Bittner, M., Offermann, D., Graef, H.-H., Donner, M., and Hamilton, K.: An 18-year time series of OH rotational temperatures and middle atmosphere decadal variations, J. Atmos. Sol.-Terr. Phys., 64, 1147–1166, 2002.

Burns, G. B., French, W. J. R., Greet, P. A., Phillips, F. A., Williams, P. F. B., Finlayson, K., and Klich, G.: Seasonal variations and inter-year trends in 7 years of hydroxyl airglow rotational temperatures at Davis station (69° S, 78° E), Antarctica, J. Atmos. Sol.-Terr. Phys., 64, 1167–1174, 2002.

Burns, G. B., Kawahara, T. D., French, W. J. R., Nomura, A., and Klekociuk, A. R.: A comparison of hydroxyl rotational temperatures from Davis (69° S, 78° E) with the sodium lidar temperatures from Syowa (69° S, 78° E), Geophys. Res. Lett., 30, 25-1:25-4, 2003.

Coxon, J. A. and Foster, S. C.: Rotational analysis of hydroxyl vibration-rotation emission bands: Molecular constants for OH $X^2\Pi$, $6 \le v \le 10$, Can. J. Phys., 60, 41–48, 1982.

Espy, P. J. and Hammond, M. R.: Atmospheric transmission coefficients for hydroxyl rotational lines used in rotational temperature determinations, J. Quant. Spectrosc. Radiat. Transfer, 54, 879–889, 1995.

Espy, P. J. and Stegman, J.: Trends and variability of mesospheric temperature at high-latitudes, Phys. Chem. Earth, 27, 543–553, 2002.

French, W. J. R., Burns, G. B., Finlayson, K., Greet, P. A., Lowe, R. P., and Williams, P. F. B.: Hydroxyl (6-2) airglow emission intensity ratios for rotational temperature determination, Ann. Geophys., 18, 1293–1303, 2000.

Gattinger, R. L. and Vallance Jones, A.: The vibrational development of the $O_2(b^1\Sigma_g^+ - X^3\Sigma_g^-)$ system in auroras, J. Geophys. Res., 81, 4789–4792, 1976.

Gattinger, R. L. and Vallance Jones, A.: Quantitative spectroscopy of the aurora, 2, the spectrum of medium intensity aurora between 4500 and 8900Å, Can. J. Phys., 52, 2343–2356, 1974.

Goldman, A.: Line parameters for the atmospheric band system of OH, Appl. Opt., 21, 2100–2102, 1982.

Golitsyn, G. S., Semenov, A. I., Shefov, N. N., Fishkova, L. M., Lysenko E. V., and Perov, S. P.: Long-term temperature trends in the middle and upper atmosphere, Geophys. Res. Lett., 23, 1741–1744, 1996.

Greet, P. A., French, W. J. R., Burns, G. B., Williams, P. F. B., Lowe, R. P., and Finlayson, K.: OH(6-2) spectra and rotational temperature measurements at Davis, Antarctica, Ann. Geophys., 16, 77–89, 1998.

Langhoff, S. R., Werner, H.-J., and Rosmus, P.: Theoretical transition probabilities for the OH Meinel system, J. Mol. Spectr., 118, 507–529, 1986.

Longhurst, R. S.: Geometrical and physicsal optics, Longmans, London, 1957.

Lysenko, E. V., Perov, S. P., Semenov, A. I., Shefov, N. N., Sukhudoev, V. A., Givishvili, G. V., and Leshchenko, L. N.: Long-term trends of the yearly mean temperature at heights from 25 to 100 km, Atmos. Oceanic Phys., 35, 435–443, 1999.

Melo, S. M. L., Takahashi, H., Clemesha, B.R., and Simonich, D.M.: An experimental study of the nighglow OH(8-3) band emission process in the equatorial mesosphere, J. Atmos. Sol.-Terr. Phys., 59, 479–486, 1997.

Mies, F. H.: Calculated vibrational transition probabilities of $OH(X^2\Pi)$, J. Mol. Spectr., 53, 150–188, 1974.

McDade, I.: The altitude dependence of the $OH(X^2\Pi)$ vibrational distribution in the nightglow: some model expectations, Planet. Space Sci., 39, 1049–1057, 1991.

Myrabo, H. K.: Temperature variation at mesopause levels during winter solstice at 78° N, Planet. Space Sci., 32, 249–255, 1984.

Osterbrock, D. E., Fulbright, J. P., Martel, A. R., Keane, M. J., Trader, S. C., and Basri, G.: Night-sky high-resolution spectral atlas of OH and O_2 emission lines for Echelle spectrograph wavelength calibration, Publ. Astron. Soc. Pac., 108, 277–308, 1996.

Osterbrock, D. E., Fulbright, J. P., and Bida, T. A.: Night-sky high-resolution spectral atlas of OH and O_2 emission lines for Echelle spectrograph wavelength calibration II, Publ. Astron. Soc. Pac., 109, 614–627, 1997.

Osterbrock, D. E. and Martel, A. R.: Sky spectra at a light-polluted site and the use of atomic and OH sky emission lines for wavelength calibration, Publ. Astron. Soc. Pac., 104, 76–82, 1992.

Pendleton, W. R., Espy, P. J., and Hammond, M. R.: Evidence for non-local-thermodynamic-equilibrium rotation in the OH nightglow, J. Geophys. Res., 98, 11 567–11 579, 1993.

Pendleton, W. R. and Taylor, M. J.: The impact of L-uncoupling on Einstein coefficients for the OH Meinel (6,2) band: implications for Q-branch rotational temperatures, J. Atmos. Sol.-Terr. Phys., 64, 971–983, 2002.

Portman, R. W., Thomas, G. E., Soloman, S., and Garcia, R. R.: The importance of dynamical feedbacks on doubled CO_2-induced changes in the thermal structure of the mesosphere, Geophys. Res. Lett., 22, 1733–1736, 1995.

Rothman, L. S., Rinsland, C. P., Goldman, A., Massie, S. T., Edwards, D. P., Flaud, J.-M., Perrin, A., Camy-Peyret, C., Dana, V., Mandin, J.-Y., Schroeder, J., McCann, A., Gamache, R. R., Wattson, R. B., Yoshino, K., Chance, K. V., Jucks, K. W., Brown, L. R., Nemtchinov, V., and Varanasi, P.: The HITRAN molecular spectroscopic database and HAWKS (HITRAN Atmospheric Workstation) 1996 edition, J. Quant. Spectrosc. Radiat. Transfer, 60, 665–710, 1998.

Rothman, L. S., Barbe, A., Benner, D. C., Brown, L. R., Camy-Peyret, C., Carleer, M. R., Chance, K., Clerbaux, C., Dana, V., Devi, V. M., Fayt, A., Flaud, J.-M., Gamache, R. R., Goldman, A., Jacquemart, D., Jucks, K. W., Lafferty, W. J., Mandin, J.-Y., Massie, S. T., Nemtchinov, V., Newnham, D. A., Perrin, A., Rinsland, C. P., Schroeder, J., Smith, K. M., Smith, M. A. H., Tang, K., Toth, R. A., Vander Auwera, J., Varanasi, P., and Yoshino, K.: The HITRAN molecular spectroscopic database: edition of 2000 including updates of 2001, J. Quant. Spectrosc. Radiat. Transfer, 82, 5–44, 2003.

Rusch, D. W., Torr, D. G., Hays, P. B., and Walker, J. C. G.: The OII (7319-7330Å) dayglow, J. Geophys. Res., 82, 719–722, 1977.

She, C. Y. and Lowe, R. P.: Seasonal temperature variations in the mesopause region at mid-latitude: comparison of lidar and hydroxyl rotational temperatures using WINDII/UARS OH height profiles, J. Atmos. Sol.-Terr. Phys., 60, 1573–1583, 1998.

Sivjee, G. G. and Hamway, R. M.: Temperature and chemistry of the polar mesopause OH, J. Geophys. Res., 92, 4663–4672, 1987.

Slanger, T. G., Cosby, P. C., Huestis, D. L., and Osterbrock, D. E.: Vibrational level Distribution of $O_2(b^1\Sigma_g^+, v=0-15)$ in the mesosphere and lower thermosphere region, J. Geophys. Res., 105(D16), 20 557–20 564, 2000.

Slanger, T. G., Huestis, D. L., Osterbrock, D. E., and Fulbright, J. P.: The isotopic oxygen nightglow as viewed from Mauna Kea, Science, 277, 1485–1487, 1997.

Slanger, T. G. and Osterbrock, D. E.: Aeronomy-astronomy collaboration focuses on nighttime terrestrial atmosphere, EOS, 79, 153–154, 1998.

Smith, R. W., Sivjee, G. G., Stewart, R. D., McCormac, F. G., and Deehr, C. S.: Polar cusp ion drift studies through high-resolution interferometry of O^+ 7320-Å emission, J. Geophys. Res., 87, 4455–4460, 1982.

Stubbs, L. C., Boyd, J. S., and Bond, F. R.: Measurement of the OH rotational temperature at Mawson, East Antarctica, Planet. Space Sci., 31, 923–932, 1983.

Takahashi, H. and Batista, P. P.: Simultaneous measurements of OH(9,4), (8,3), (7,2), (6,2) and (5,1) bands in the airglow, J. Geophys. Res., 86, 5632–5642, 1981.

Takahashi, H., Clemesha, B. R., and Sahai, Y.: Nightglow OH(8-3) band intensities and rotational temperatures at 23° S, Planet. Space Sci., 22, 1323–1329, 1974.

Turnbull, D. N. and Lowe, R. P.: Vibrational population distribution in the hydroxyl night airglow, Can. J. Phys., 61, 244–250, 1983.

Turnbull, D. N. and Lowe, R. P.: New hydroxyl transition probabilities and their importance in airglow studies, Planet. Space Sci., 37, 723–738, 1989.

Wallace, L., Hinkle, K., and Livingston, W.: An atlas of the spectrum of the solar photosphere from 13,500 to 28,000 cm^{-1} (3570 to 7405 Å), ftp://nsokp.nso.edu/pub/atlas/visatl/, N.S.O. Technical Report #98-001, 1998.

Wang, J., Cole, H. L., Carlson, D. J., Miller, E. R., Beierle, K., Paukkunen, A., and Laine, T. K.: Corrections of humidity measurement errors from the Vaisala RS80 radiosonde – applications to TOGA COARE data, J. Atmos. Oceanic Technol., 19, 981–1001, 2002.

Williams, P. F. B.: OH rotational temperatures at Davis, Antarctica, via scanning spectrometer, Planet. Space Sci., 44, 163–170, 1996.